PULSED FIELD GRADIENT NMR STUDY OF SORBATE TRANSPORT IN CARBON MOLECULAR SIEVES AND SBA-16 MATERIALS

By

ROHIT KANUNGO

A THESIS PRESENTED TO THE GRADUATE SCHOOL
OF THE UNIVERSITY OF FLORIDA IN PARTIAL FULFILLMENT
OF THE REQUIREMENTS FOR THE DEGREE OF
MASTER OF SCIENCE

UNIVERSITY OF FLORIDA

2011

“To my mom, dad and brother”

ACKNOWLEDGMENTS

I express my sincere thanks and gratitude towards my esteemed research advisor Dr. Sergey Vasenkov for his constant encouragement and inspiring guidance. I have learned a lot while working under him. I will like to thank my project collaborators Mr. Robert Mueller and Mr. Sen-Ming Wang for their immense help and support. Discussions with them always gave me new perspective and ideas. I will also thank my lab mates Ms. Aakanksha Katihar & Mr. Eric Hazelbaker for their company and friendship. I am grateful to the staff at Advanced Magnetic Resonance Imaging and Spectroscopy (AMRIS) facility for being very helpful while conducting measurements. Special thanks to Dr. Daniel Plant for his technical support and valuable advice. Lastly, I like to thank Dr. Peng Jiang for being a committee member for my Master's research.

My family has been a great inspiration to me. They taught me, guided me and always helped me in selecting the right path. I am very thankful to my mom and dad for always supporting me.

TABLE OF CONTENTS

page

ACKNOWLEDGMENTS 4

LIST OF TABLES 7

LIST OF FIGURES 8

LIST OF ABBREVIATIONS 9

ABSTRACT 11

CHAPTER

1 INTRODUCTION 12

Molecular Transport in Porous Materials 12
Basics of Diffusion 12
Basics of NMR 15
Longitudinal & Transverse Magnetization 16
Relaxation 17
Signal Detection 18
Pulsed Field Gradient (PFG) NMR 18
PFG NMR Stimulated Echo Longitudinal Encode-Decode Pulse Sequence 19
PFG NMR Stimulated Echo with Bipolar Gradients Pulse Sequence 23
Generalized Attenuation Equation 24

2 TRANSPORT IN SBA-16 MATERIALS 25

Motivation 25
Experimental Details 25
Materials and Sample Preparation 25
PFG NMR Measurements Details 28
^{13}C PFG NMR Measurements 29
^{1}H PFG NMR Measurements 29
Results and Discussion 30
Work in Progress 35

3 TRANSPORT IN CARBON MOLECULAR SIEVES 36

Motivation 36
Experimental Details 37
Materials and Sample Preparation 37
PFG NMR Measurements Details 38
Results and Discussion 39
Work in Progress 44

LIST OF REFERENCES 45

BIOGRAPHICAL SKETCH 47

LIST OF TABLES

Table page

2-1 Textural properties for SBA-16 materials obtained from the measurements of the nitrogen adsorption/desorption isotherms 26

2-2 Results of the fitting of ^{13}C and ^{1}H PFG NMR attenuation curves for methyl oleate diffusion in SBA-16 materials 33

3-1 Results of the fitting of ^{13}C and ^{1}H PFG NMR attenuation curves for methane diffusion in CMS 43

LIST OF FIGURES

Figure page

1-1 Schematic picture showing behavior of spins in the presence of external magnetic field 16

1-2 Schematic representation of spin precession in presence of an external magnetic field and after application of $\pi/2$ r.f. pulse..... 17

1-3 Schematic of the PFG NMR stimulated echo longitudinal encode-decode or longitudinal eddy current delay pulse sequence 19

1-4 Schematic of the PFG NMR stimulated echo pulse sequence with bipolar gradients..... 23

2-1 SEM images of samples of SBA-16-130 (a), SBA-16-100 (b), SBA-16-80 (c), SBA-16-60 (d)..... 27

2-2 PFG NMR attenuation curves measured for diffusion of methyl oleate in the sample of SBA-16-130 32

3-1 Examples of PFG NMR attenuation curves measured for methane diffusion in 6FDA/BPDA(1:1) -DAM CMS using proton and ^{13}C PFG NMR 40

3-2 Dependences of the methane self-diffusion coefficient on the root MSD 41

3-3 Temperature dependences of the methane self-diffusion coefficient..... 42

LIST OF ABBREVIATIONS

BET	BET adsorption isotherm
CMS	Carbon molecular sieves
FID	Free Induction Decay
MRI	Magnetic Resonance Imaging
MSD	Mean square displacement
NMR	Nuclear Magnetic Resonance
PFGNMR	Pulsed Field Gradient Nuclear Magnetic Resonance
PGSTE-LED	PFG NMR stimulated echo longitudinal endode decode pulse sequence
r.f. pulse	Radio frequency pulse
SBA16	Santa Barbara Amorphous materials type 16;
SEM	Scanning Electron Microscopy
TEM	Transmission Electron Microscopy
B_0	The amplitude of the applied external static magnetic field
B_1	The amplitude of the oscillating applied magnetic field due to a radio frequency pulse
c	Concentration of molecules
D	Diffusion coefficient
E	Activation energy for diffusion
g	Amplitude of magnetic field gradient
J	Flux of molecules or ions
m_i	Amplitude of magnetic moment due to individual spin
M_{X-Y}	Amplitude of net transverse magnetization
M_z	Amplitude of net magnetization along z axis

M_0	Equilibrium value of net magnetization along z axis
P	Probability density
r	Radial coordinate of position of molecule/nuclear spin in spherical coordinate system
$\langle r^2 \rangle$	Mean square displacement
R	Gas constant
t	Time
t_{eff}	Effective diffusion time
T	Absolute temperature
T_1	Longitudinal NMR relaxation time
T_2	Transverse NMR relaxation time
T_{LED}	Duration between the fourth and fifth r.f. pulse in PGSTE-LED pulse sequence for eddy current dissipation
z	z coordinate of position of molecule/ nuclear spin
γ	Gyromagnetic ratio
δ	Duration of magnetic field gradient pulse
Δ	Diffusion time
τ_1	Duration between the first and second r.f. pulse in PFG NMR stimulated echo pulse sequence
τ_2	Duration between the second and third r.f. pulse in PFG NMR stimulated echo pulse sequence
ψ	Amplitude of signal attenuation in PFG NMR experiment
ω_0	Larmor frequency

Abstract of Thesis Presented to the Graduate School
of the University of Florida in Partial Fulfillment of the
Requirements for the Degree of Master of Science

PULSED FIELD GRADIENT NMR STUDY OF SORBATE TRANSPORT IN CARBON MOLECULAR SIEVES AND SBA-16 MATERIALS

By

Rohit Kanungo

December 2011

Chair: Sergey Vasenkov
Major: Chemical Engineering

This work presents results of diffusion studies of sorbate molecules in selected microporous and mesoporous materials at various length scales of displacements. The materials investigated were carbon molecular sieve (CMS) membranes and BTEB (viz., 1, 4-bis (triethoxysilyl)-benzene) SBA-16. CMS membranes show promise for applications in separations of mixtures of small gas molecules, while SBA-16 can be used as an active and selective catalyst in bio-diesel production. For both types of applications diffusion of guest molecules in the micropore networks of these materials is expected to play an important role. Diffusion studies were performed by a pulsed field gradient (PFG) NMR technique that combines advantages of high field (17.6 T) NMR and high magnetic field gradients (up to 30 T/m). This technique has been recently introduced at the University of Florida in collaboration with the National Magnet Lab. In addition to a more conventional proton PFG NMR, also ^{13}C PFG NMR was used.

CHAPTER 1
INTRODUCTION

Molecular Transport in Porous Materials

Porous materials have many industrial applications in which transport of sorbate molecules at very small, i.e. micrometer or sub-micrometer length scales play a vital role. In many cases macroscopic properties are controlled by transport properties at such small length scales[1]. Porous membranes and catalysts often contain interconnected networks of pores of different sizes, i.e. networks of micropores with pore sizes approaching the sizes of molecules and much larger meso and/or macropores. In recent years there has been significant progress in the area of sorbate diffusion where pore systems have uniform or similar pore sizes. However, understanding of molecular transport in heterogeneous systems, where network of pores with different non-uniform pore sizes are present, is rather limited.

This thesis reports investigation of self-diffusion on various relevant length scales with the help of pulsed field gradient NMR. Such investigation allowed obtaining detailed information about transport properties in carbon molecular sieves and SBA-16 materials.

Basics of Diffusion

Diffusion process can be defined as a random, thermal motion of molecules and can be described by two basic modes: transport diffusion and self-diffusion. Transport diffusion involves the movement of molecules in order to eliminate macroscopic gradients of chemical potential (which was earlier understood to be concentration gradient) while self-diffusion occurs in the absence of macroscopic concentration or chemical potential gradients. The transport diffusion coefficient describes the

relationship between the flux of molecules and a concentration gradient under non-equilibrium conditions. According to the Fick's first law[2,3] of diffusion, mass flux J in z direction can be written as

$$J = -D\frac{\partial c}{\partial z}, \tag{1.1}$$

where $c(z)$ is their concentration, and D is the corresponding diffusion coefficient. For small molecular concentration D is often independent of concentration but it can be a function of the concentration at large concentrations. Application of Equation 1.1 in combination with the mass balance written for an elementary volume element leads to the Fick's second law of diffusion

$$\frac{\partial c}{\partial t} = \frac{\partial\left[D(c)\frac{\partial c}{\partial z}\right]}{\partial z}. \tag{1.2}$$

For the case where D is independent of concentration, the above equation simplifies to

$$\frac{\partial c}{\partial t} = D\frac{\partial^2 c}{\partial z^2}. \tag{1.3}$$

Self-diffusion is the random translational motion of molecules driven by thermal energy which occurs in the absence of a macroscopic gradient of chemical potential. If one considers an uneven distribution of labeled and unlabeled molecules under conditions when overall molecular concentration remains the same at each point of the considered volume, the self-diffusion coefficient can be derived from the Fick's First Law. The diffusive flux J^* of labeled molecules can be written is

$$J^* = -D_s\frac{\partial c^*}{\partial z}\Big|_{c=const.}, \tag{1.4}$$

where c^* is the concentration of the labeled molecules and D_s is self diffusivity. For a general case of one, two or three dimension Equation 1.4 can be written as

$$J(r,t) = -D_s \nabla c(r,t), \tag{1.5}$$

where D_s is the self-diffusion coefficient, r is the position in space, t is the time and $c(r,t)$ is the concentration of (labeled) molecules moving in one, two, or three dimensional space. Similarly Fick's second law for the labeled molecules can be written as

$$\frac{\partial c(r,t)}{\partial t} = \nabla.(D_s \nabla c(r,t)). \tag{1.6}$$

Thermal stochastic motion of molecules will cause the concentration gradient to approach the zero value with increasing diffusion time. Since overall molecular concentration remains the same for all positions, the self-diffusion coefficient D_s in equation can be placed before the first gradient operator. Equation 1.6 can be solved by replacing the spatially-dependent concentration term with a term describing the probability that a molecule will diffuse from its initial position r_0 to the position r after time t. The solution gives a Gaussian distribution that is also known as diffusion propagator[4].

$$P(r_0,r,t) = \frac{1}{(4\pi Dt)^{3/2}} exp\left\{\frac{-(r-r_0)^2}{4Dt}\right\}, \tag{1.7}$$

where $P(r_0,r,t)$ is the probability that a molecule with an initial position, r_0, will migrate to a final position, r, after time t and D is the self diffusivity. The Einstein relation[5] can be easily derived from the diffusion propagator (Equation 1.7)

$$\langle r^2(t)\rangle = 6Dt, \tag{1.8}$$

where $\langle r^2(t)\rangle$ is the mean square displacement (MSD) in the case of 3-dimensional diffusion. This equation offers another way of defining self-diffusion coefficients of molecules.

Basics of NMR

Nuclear magnetic resonance (NMR) is a physical phenomenon in which magnetic nuclei in a magnetic field absorb and re-emit electromagnetic radiation. This energy is at a specific resonance frequency which depends on the strength of the magnetic field and the magnetic properties of atomic nuclei. NMR allows the observation of specific quantum mechanical magnetic properties of the atomic nucleus. Many scientific fields exploit NMR phenomena to study molecular physics, crystals, and non-crystalline materials through NMR spectroscopy. NMR is also routinely used in advanced medical imaging techniques, such as in magnetic resonance imaging (MRI).

Atomic nuclei possess a quantum-mechanical property called spin angular momentum or spin. It is actually an intrinsic property of elementary particles, including protons and neutrons making up atomic nuclei. Nuclei with non-zero spin angular momentum also have an intrinsic magnetic moment and hence are called magnetically active. In the absence of any external magnetic field the distribution of spin-polarization axes and corresponding magnetic moments of individual nuclei in a macroscopic sample is completely isotropic. Therefore, net nuclear magnetization in the sample is zero (Figure 1-1a). However, when an external magnetic field is applied, it exerts a torque on the nuclear magnetic moment of individual nuclei and causes the spin polarization to move on a cone always keeping the same angle between the directions of magnetic moment and the field (Fig 1-2a). Such type of motion is known as precession The frequency of precession which is referred to as the Larmor frequency[6,7] is given by

$$\omega_0 = -\gamma B_{0,} \tag{1.9}$$

where γ is the gyromagnetic ratio of the nucleus under observation and and B_0 is the amplitude of static magnetic field.

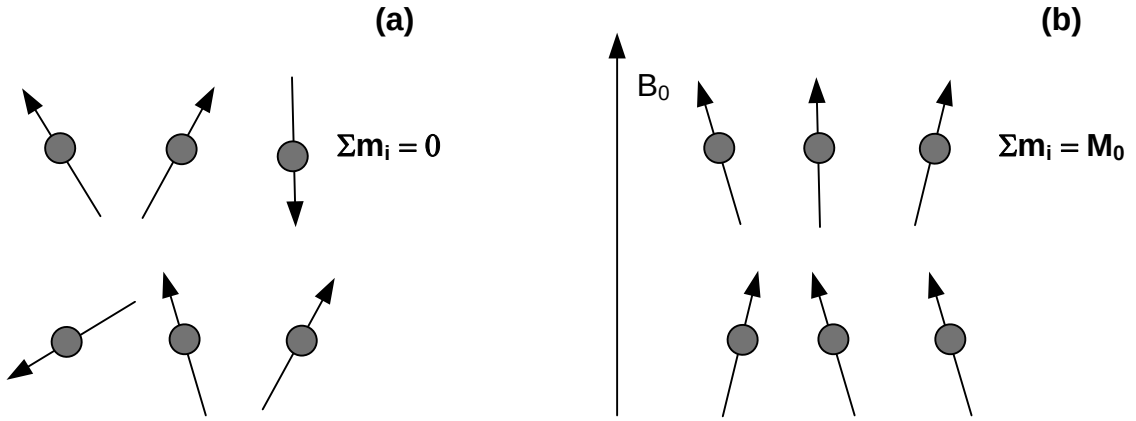

Figure 1-1. (a) Schematic picture showing that in the absence of external magnetic field, the net magnetic moment is zero; (b) Schematic picture showing that in the presence of external magnetic field a net longitudinal magnetization is developed. The longitudinal magnetization M_0 is the vector sum of individual magnetic moments m_i[8].

Longitudinal & Transverse Magnetization

In the absence of external magnetic field the spin polarizations of the sample is isotropic. As a result, there is no net magnetization in the sample. On application of external magnetic field, the isotropy of spin polarizations break and a thermal equilibrium is reached, which results in the formation of a net macroscopic nuclear magnetization in the sample along the direction of the applied magnetic field (Fig 1-1b). This direction is also referred to as the longitudinal direction.

In NMR, nuclear magnetization is detected in a plane perpendicular to longitudinal direction. This is achieved by application of additional oscillating magnetic field B_1 in the direction normal to the direction of static magnetic field B_0. The frequency of the B_1 field is kept sufficiently close to the Larmor frequency resulting in resonance phenomenon Since Larmor frequency is in range of radio frequency (r.f.), application of B_1 field is also

referred to as application of an r.f. pulse in NMR jargon. The duration of r.f. pulse can be chosen in such a way that it tilts the net magnetization by 90°. Once r.f. pulse is turned off, the direction of the net magnetization gradually returns to the direction of the static external magnetic field B_0 due to a relaxation process.

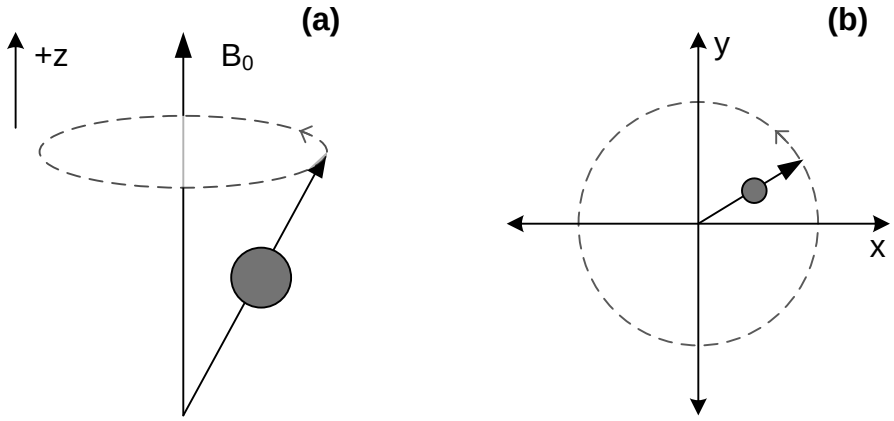

Figure 1-2. (a) Schematic representation of spin precession in presence of an external magnetic field, (b) After application of $\pi/2$ r.f. pulse, the transverse magnetization precesses in the transverse plane with Larmor frequency ω_0.

Relaxation

The process of returning of the net nuclear magnetization to its equilibrium state is referred to as NMR relaxation. Two types of NMR relaxation can be distinguished: 1) T_2 (Transverse) relaxation and 2) T_1 (Longitudinal) relaxation[7-9].

T_2 NMR relaxation is the process that arises due to the decay of transverse magnetization to zero. This decay occurs due to the perturbations of the local magnetic field by neighboring nuclear spins and electronic clouds and due to the fluctuating microscopic magnetic field. The net rate of transverse relaxation can be characterized by a time constant T_2, as shown in the following equation

$$M_{X-Y}(t) = M_{X-Y}(0) \times exp\left(-\frac{t}{T_2}\right), \quad (1.10)$$

where $M_{X-Y}(t)$ is the net transverse magnetization at time t and T_2 is the Transverse NMR relaxation time.

T_1 NMR relaxation is a process that concerns with the gradual growth of the net nuclear magnetization to its equilibrium value along the $+z$ direction in the presence of a static magnetic field. After the application of 90° r.f. pulse the net magnetization grows along the z-direction and for which rate of growth can by characterized by

$$M_Z(t) = M_0\left(1 - exp(-t/T_1)\right), \quad (1.11)$$

where $M_Z(t)$ is the net longitudinal magnetization at time t , M_0 is the net equilibrium magnetization, which points along $+z$ direction. The Equation 1.11 holds for the cases when the net longitudinal magnetization is equal to zero at $t = 0$, in presence of an external magnetic field.

Signal Detection

The precessing transverse magnetization after application of a radio frequency pulse oscillates at a very well-defined frequency. This rotating magnetic moment generates an electric field due to which an oscillating electric current flow in the signal detection coil placed near the sample. The oscillating electric current induced by the precessing nuclear transverse magnetization is called the NMR signal or free-induction decay (FID).

Pulsed Field Gradient (PFG) NMR

Pulsed-field gradient NMR spectroscopy allows for direct measurements of mean square displacement (MSD) as well as of the related diffusivity and the diffusion propagator. PFG NMR exploits the fact the Larmor frequency of the precession of the

nuclear spins is field dependent. Application of a gradient of magnetic field along the z direction allows for the labeling of the positions of nuclear spins along this direction based on their Larmor frequency. In PFG NMR, a gradient of magnetic field along the z direction is applied when the net nuclear magnetization is in the transverse plane. The Larmor frequency of precession under the influence of magnetic field gradient is given by

$$\omega = -\gamma(B_0 + gz), \tag{1.12}$$

where ω is the Larmor frequency, γ is the gyromagnetic ratio, B_0 denotes the amplitude of the static external magnetic field along the $+z$ direction and g is the linear gradient of the magnetic field superimposed on the B_0 field and z is the spatial coordinate along the Z axis. Equation 1.12 shows that application of the magnetic field gradients thus makes the Larmor frequency to be position dependant, effectively labeling the nuclear spins based on their spatial coordinate along the z-direction.

PFG NMR Stimulated Echo Longitudinal Encode-Decode Pulse Sequence

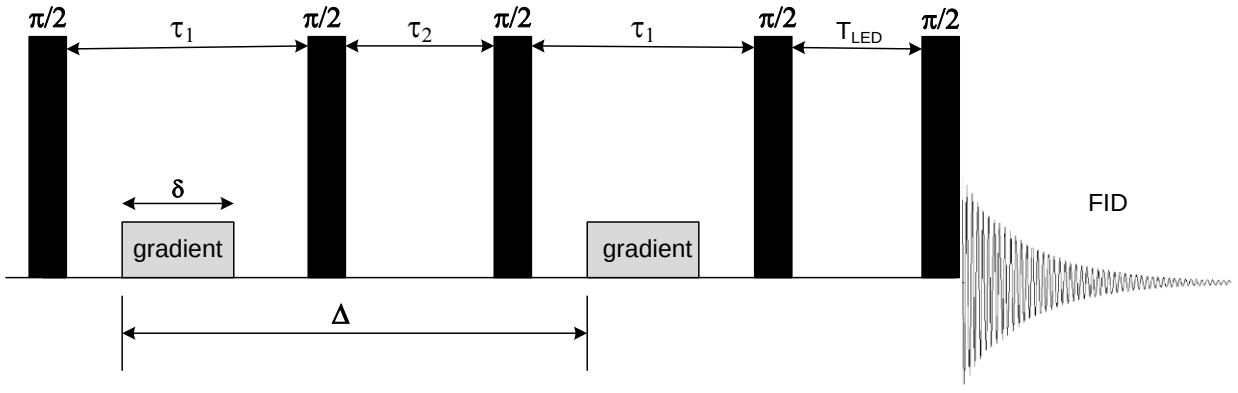

Figure 1-3. Schematic of the PFG NMR stimulated echo longitudinal encode-decode or longitudinal eddy current delay pulse sequence (PGSTE-LED)[10,11].

In PFG NMR pulse sequences, magnetic field gradient is applied during at least two short time intervals, when magnetization is in the transverse plane. Figure 1-3

shows schematic presentation of the PFG NMR stimulated echo longitudinal encode-decode or longitudinal eddy current delay pulse sequence (PGSTE-LED)[10,11]. This sequence is a modified version of the PFG NMR stimulated echo pulse sequence[12,13] (PGSTE).

This sequence consists of five r.f. ($\pi/2$) pulses. First r.f. pulse is followed by application of a field gradient of amplitude g and duration δ. The first r.f. pulse brings the longitudinal magnetization to the transverse plane. All nuclear spins experience the same magnetic field and precess at the same Larmor frequency up till this point. Hence, the initial phase of all the spins in the transverse plane can be assumed to be equal to zero. Application of the first field gradient pulse makes the Larmor frequency of spins at various positions in the sample to precess at different rates. As a result, the individual spin magnetization vectors that contribute to the net transverse magnetization de-phase. Due to de-phasing the amplitude of the net transverse magnetization is reduced. The time between the first and second gradient (Δ) is fixed and is approximately equal to the effective diffusion time of the measurement. The second $\pi/2$ r.f. pulse orients the net magnetization from the transverse plane to the –z axis. Third $\pi/2$ r.f. pulse again tilts the magnetization from the –z axis back to the transverse plane. The combination of the second and third pulses invert the accumulated phase differences in the transverse plane, such that for any pair of spins the positive phase differences becomes negative and vice versa[14-17]. After third $\pi/2$ r.f. pulse, the magnetic field gradients of the same duration and amplitude are applied again. Due to self-diffusion of molecules, the positions of nuclear spins change and the applications of the gradient pulses thus do not refocus the transverse magnetization. As a result, the extent of the decrease of the

intensity of the refocused transverse magnetization contains information about the mean square displacements of the molecules.

A quantitative treatment of the experiment to relate the signal attenuation to the molecular diffusion can be carried out by determining the net phase accumulated by individual spins and using this phase to calculate the vector sum of individual magnetic moments by the end of pulse sequence. The projection of the individual magnetization vectors on the direction that coincides with that of the transverse magnetization immediately after the application of first $\pi/2$ r.f. pulse is proportional to the cosine of the phase of nuclear spins. A further treatment uses the diffusion propagator $P(z_2, z_1, \Delta)dz_2$, which gives probability that a molecule initially at the position z_1 can be found after time Δ at a position with the coordinates between z_2 to $z_2 + dz_2$ to calculate the net transverse magnetization at the end of the pulse sequence. This allows one to derive the expression for the signal attenuation ψ for the case of normal (i.e. Fickian) diffusion

$$\psi(\delta g, t_{eff}) = exp\left(-(\gamma g \delta)^2 D t_{eff}\right), \tag{1.13}$$

where the effective diffusion time denoted by t_{eff} is given by $t_{eff} = \Delta - \delta/3$

Substituting Einstein relation (Equation1.11) into Equation 1.13 gives

$$\psi(\delta g, t_{eff}) = exp\left(-(\gamma g \delta)^2 \frac{\langle r^2 \rangle}{6}\right), \tag{1.14}$$

where $\langle r^2 \rangle / 6$ is the mean square displacement for isotropic three-dimensional diffusion in a homogeneous medium where diffusion coefficient is expected to be the same in all directions.

Typically, in a PFG NMR experiment the signal attenuation ψ is recorded as a function of the square of the field gradient strength g under the conditions when all the

other parameters of the pulse sequence are kept constant. Such dependencies of ψ on g^2 are referred to as the attenuation curves. The attenuation curves allow for a direct determination of the mean square displacements and the corresponding diffusivities using the equations of the type Equation 1.13-1.14.

This sequence offers a particular advantage for PFG NMR diffusion studies of materials, which exhibit shorter longitudinal T_1 relaxation than transverse T_2 relaxation, i.e. $T_1 > T_2$. For this sequence the signal is reduced due to T_2 relaxation only during the two time intervals of duration τ_1,when the magnetization is in the transverse plane. The diffusion time Δ can be increased in this sequence in a broad range by increasing the time interval τ_2. This provides a possibility to perform PFG NMR diffusion measurements on systems/materials using diffusion times much larger than T_2 NMR relaxation times.

PGSTE-LED contains two additional $\pi/2$ r.f. pulses separated by the time T_{LED} at the end of the sequence. The function of these two pulses is to change the direction of the net magnetization from the transverse plane to the longitudinal plane (along –z) for the time interval T_{LED} and then bring it back to the transverse plane for detection. The modification is introduced to shield the acquired signal from disturbing effects of the eddy currents generated due to rapid gradient switching. When field gradient pulses (especially high-amplitude pulses) are switched on or off, the changing magnetic field can introduce eddy currents in the gradient coils which, in turn, cause magnetic field inhomogeneity. Such field inhomogeneity is undesirable during signal detection and can be avoided by increasing the time delay between the end of second field gradient pulse and the beginning of acquisition, to allow for eddy current dissipation. PGSTE-LED

sequence addresses this problem by taking the net magnetization from the transverse plane to the longitudinal direction (-z) axis, which is followed by a delay T_{LED} for eddy current dissipation. This delay is known as the LED delay. Signal is reduced only due to T_1 NMR relaxation during the LED delay. PGSTE-LED sequence thus offers a clear advantage over the PFG NMR stimulated echo pulse sequence under the measurement conditions characterized by short T_2 NMR relaxation times coupled with the need for large field gradients, which are likely to introduce disturbing eddy currents.

PFG NMR Stimulated Echo with Bipolar Gradients Pulse Sequence

Figure 1-4 shows a schematic for the PFG NMR stimulated echo pulse sequence with bi-polar gradients[18-21], i.e. the 13-interval sequence.

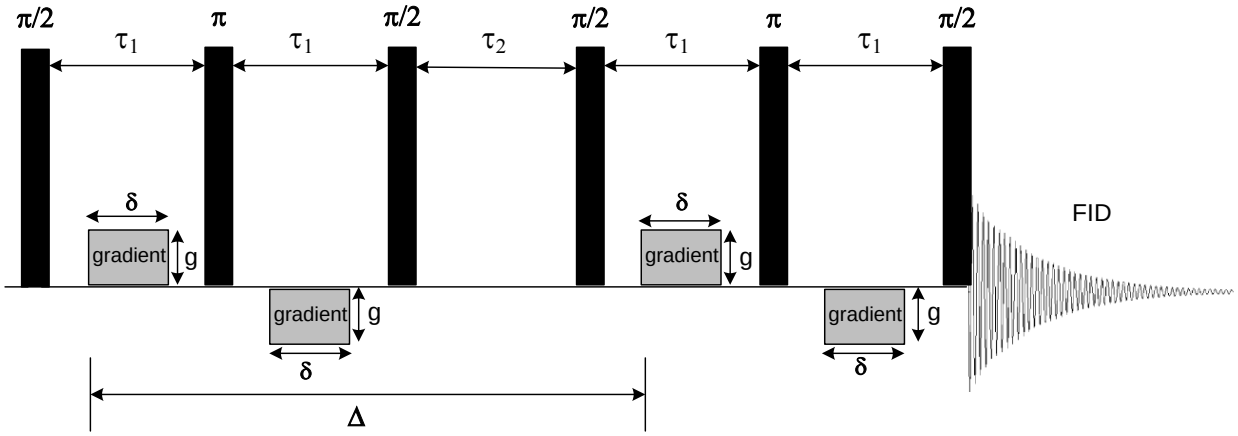

Figure 1-4. Schematic of the PFG NMR stimulated echo pulse sequence with bipolar gradients. This pulse sequence uses bipolar gradients to suppress artifacts due to magnetic susceptibility, also referred to as internal gradients.

This sequence gives advantage when the sample is characterized by different magnetic susceptibilities in different locations within the sample. This may lead to extra attenuation of the signal and can introduce systematic artifacts in the measurements of self-diffusion. Alternating pulsed-field gradients are used to suppress susceptibility-induced artifacts in diffusion experiments For the case of an isotropic normal diffusion

the expression for the signal attenuation using the 13-interval pulse sequence is given by[19]

$$\psi(\delta g, t_{eff}) = exp(-(2\gamma g\delta)^2 Dt_{eff}), \quad (1.15)$$

where t_{eff} is the effective diffusion time given by $t_{eff} = \Delta - {}^{\tau}/_{2} - {}^{\delta}/_{6}$.

Generalized Attenuation Equation

The general form of attenuation equation for normal isotropic diffusion used for all the pulse sequences discussed above can be simplified to the following form

$$\psi(\delta g, t_{eff}) = exp(-(q)^2 Dt_{eff}), \quad (1.16)$$

where $q = \gamma g\delta$ for PGSTE-LED pulse sequence and $q = 2\gamma g\delta$ for the 13-interval pulse sequence. The effective diffusion time $t_{eff} = \Delta - {}^{\delta}/_{3}$ for PGSTE-LED and $t_{eff} = \Delta - {}^{\tau}/_{2} - {}^{\delta}/_{6}$ for the 13-interval sequence. In the case where the PFG NMR sample contains n ensembles of molecules, each diffusing with a unique characteristic diffusivity, the attenuation equation can be expressed as a summation of several weighted exponential terms

$$\psi(\delta g, t_{eff}) = \sum_{i}^{n} p_i exp(-(q)^2 D_i t_{eff}), \quad (1.17)$$

where p_i is the fraction of i^{th} ensemble of molecules.

CHAPTER 2
TRANSPORT IN SBA-16 MATERIALS

SBA-16 is a porous silica with large (5-15 nm) cage-like mesopores arranged in a three dimensional cubic body-centered $Im\bar{3}m$ symmetry[22,23]. Electron crystallography studies[24] for SBA-16 suggest that each mesopore is connected to eight neighboring mesopores by microporous channels. These materials are of high interest for their application in catalysis. This thesis reports the PFG NMR results for diffusion of methyl oleate molecules in the BTEB (viz., 1, 4-bis (triethoxysilyl)-benzene) SBA-16 materials.

Motivation

The existence of a 3-dimensional system of relatively large pores makes mesoporous silica of the SBA-16 type an attractive candidate as a catalyst support for catalytic production of biodiesel, viz. fatty acid methyl esters. Using these materials for the catalytic production of biodiesel from triglycerides, which can be extracted from marine algae, shows potential for addressing increasing needs in fuels. Understanding transport properties of such relatively large sorbate molecules in the pore system of SBA-16 is of high importance for catalysis in this type of materials. The diffusion studies were performed using pulsed field gradient (PFG) NMR. In addition to traditional ^{1}H PFG NMR, ^{13}C PFG NMR was also used to obtain quantitative knowledge of methyl oleate self-diffusion inside BTEB SBA-16 particles.

Experimental Details

Materials and Sample Preparation

Four samples of mesoporous silica SBA-16 were supplied by the research group of Dr. Serge Kaliaguine from Université Laval, Canada. The samples were synthesized using the procedure reported by Cho et al.[11] The four samples are primarily distinguished from

each other due to a difference in the pore sizes. Such difference was a consequence of using different temperatures for hydrothermal treatment (aging). The samples are denoted as SBA-16-*T* with the aging temperature *T* expressed in degrees Celsius. Sample characterization data (SEM and TEM) was provided to us by research group of Dr. Dong Yan Zhao, Fudan University. Table 2-1 shows the data obtained from Nitrogen adsorption/ desorption isotherms provided by Dr. Serge Kaliaguine's group.

Table 2-1. Textural properties for SBA-16 materials obtained from the measurements of the nitrogen adsorption/desorption isotherms.

	S_{BET} m^2g^{-1}	S_{DFT} m^2g^{-1}	V_t cm^3g^{-1}	V_{DFT} cm^3g^{-1}	V_{mic} cm^3g^{-1}	Dp_{des} nm	Dp_{adsBJH} nm	Dp_{DFT} nm
SBA-16-130	830	758	0.74	0.64	0.13	3.6	7.1	10.5 (1.4)
SBA-16-100	677	694	0.53	0.48	0.14	3.5	6.2	9.4(1.4)
SBA-16-80	452	498	0.39	0.32	0.10	3.3	5.0	8.2(1.4)
SBA-16-60	415	429	0.31	0.27	0.08	3.3	4.7	8.1(1.3)

S_{BET} is the nitrogen BET specific surface area calculated from the isotherm analysis in the relative pressure range of 0.10-0.20; S_{DFT} is the specific surface area estimated using the NLDFT method. V_t is the total pore volume at relative pressure 0.97.; V_{DFT} is the total pore volume, $V_{mic,}$ is the total micropore volume, Dp_{des} is evaluated using the desorption branch, Dp_{adsBJH} is the pore size getting from adsorption BJH, D_{PDFT} is the primary mesopore cage diameter estimated using the NLDFT method.

Table 2-1 shows results of the characterization of textural properties of the samples. The data in the table were obtained from the measurements of the nitrogen adsorption/desorption isotherms (not shown). These data indicate that in SBA-16-130 the diameter of the primary mesopores is largest and the thickness of the walls separating these mesopores is smallest in comparison to other samples. The mean particle sizes, as estimated from SEM of samples (Figure 2-1), for SBA-16-130, SBA-16-100, SBA-16-80 and SBA-16-100 are 3 μm, 2 μm, 6 μm, and 4 μm respectively.

PFG NMR samples were prepared in a 5 mm NMR tube. Around 50 mg of SBA-16 was introduced in NMR tube. The NMR tube was connected to a custom made vacuum system and samples were activated under high vacuum at around 380 K for 24 hours. Activated sample was separated from vacuum system and then methyl oleate (99.9% purity) was added to the sample. The sorbate quantity was just sufficient to ensure that the bed of SBA-16 particles is completely covered with the liquid sorbate. This is done to ensure that all mesopores and micropores of the SBA-16 particles are filled with the sorbate. Upon loading, the NMR tube was flame sealed.

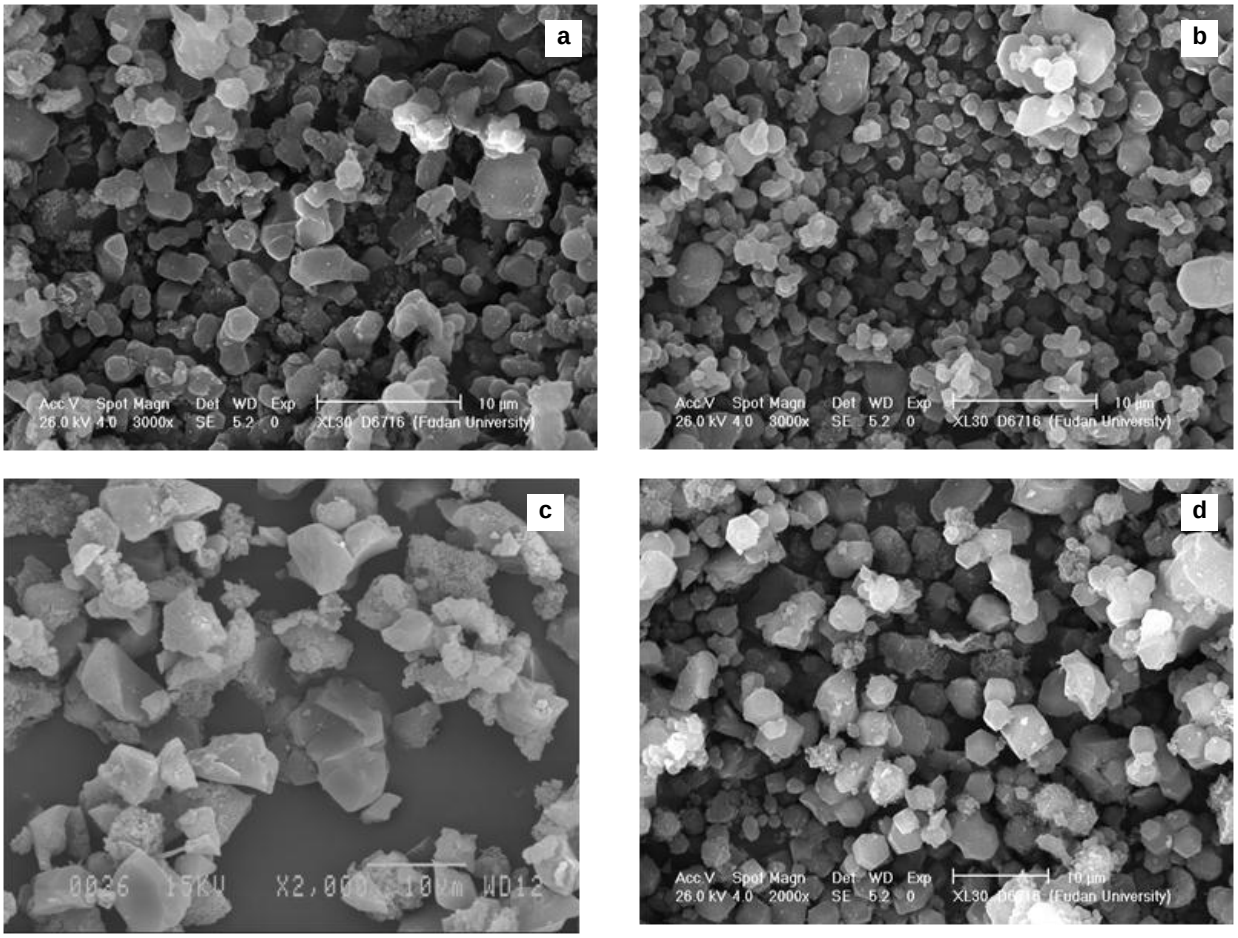

Figure 2-1. SEM images of samples of SBA-16-130 (a), SBA-16-100 (b), SBA-16-80 (c), SBA-16-60 (d).

PFG NMR Measurements Details

Diffusion studies were performed by proton and ^{13}C PFG NMR using a wide-bore 17.6 T Bruker BioSpin spectrometer. Magnetic field gradients with the amplitude up to 30 T/m were generated using diff60 diffusion probe and Great60 gradient amplifier (Bruker BioSpin). Diffusion measurements were carried out using 13-interval PFG NMR sequence with bipolar gradients[18-22] and PFG NMR stimulated echo sequence with the longitudinal eddy current delay (PGSTE LED)[22,25]. Since susceptibility effects were not expected while performing ^{13}C PFG NMR (low γ) measurements, PGSTE LED sequence was used for diffusion measurement. PGSTE LED signal is less affected by T_2 NMR relaxation as compared to 13-interval sequence. With proton PFG NMR measurements 13-interval sequence was used to avoid any susceptibility effects in diffusion measurements. Due to abundant signal from proton NMR the signal reduction due to T_2 NMR relaxation affects was not significant. In both measurements, NMR spectra of the sorbate consisted of a single line. It was verified that the line shape does not depend on the gradient amplitude. Effective diffusivities D_i were obtained from biexponential/triexponential fit of PFG NMR attenuation curves using Equation 1.17. The estimated fraction of the sorbate inside the meso- and micropores of the SBA-16 particles for all samples was in between 7% and 15% of the total sorbate added.

This thesis reports PFG NMR diffusion results only for SBA-16-130 material. Diffusion studies of the other SBA-16 samples listed in Table 2-1 are in progress.

^{13}C PFG NMR Measurements

Values of gradient duration δ and effective diffusion time t_{eff} were kept constant for measurement for each attenuation curve. Measurements were performed at different diffusion times but maximum effective diffusion time was restricted to 38.7 ms due to poor signal to noise ratio at higher diffusion times. The maximum gradient amplitude was around 26 T/m and the gradient duration was around1.5 ms. The duration between first and second $\pi/2$ r.f pulses of the PGSTE-LED sequences was between 3 and 4 ms. Transverse (T_2) NMR relaxation time for ^{13}C PFG NMR was found to be in the range between 11 and 16 ms for the sorbate fraction inside the pores. For bulk sorbate it was found to be between 51 and 77ms. The T_2 NMR relaxation times were determined using the standard Carr-Purcell-Meiboom-Gill (CPMG) sequence[15,22]. The corresponding values of the longitudinal (T_1) NMR relaxation times were between 650 and 750ms. These values were measured by the standard inversion recovery sequence and correspond to bulk sorbate. T_1 relaxation times of sorbate inside the pores could not be measured because the contribution of this sorbate fraction to the total NMR signal was relatively small. C-13 PFG NMR measurements gave an advantage of measuring diffusivities at very low length scales.

^{1}H PFG NMR Measurements

As in ^{13}C PFG NMR measurements, values of gradient duration δ and effective diffusion time t_{eff} were kept constant for measurement for each attenuation curve. Effective diffusion times of up to 255.3 ms were used in these measurements. The maximum gradient amplitude was around 26 T/m and the gradient duration was varied between 0.6 ms and 1.0 ms. The duration between the first and second $\pi/2$ r.f pulses of

the 13-Interval sequence was 3.2 ms. Transverse (T_2) NMR relaxation time for proton PFG NMR was determined using the standard Carr-Purcell-Meiboom-Gill (CPMG) sequence[15,22]. It was found to be 3 ms for the sorbate fraction inside the pores and 60 ms for the bulk sorbate. The corresponding values of the longitudinal (T_1) NMR relaxation times were 49 ms for sorbate fraction inside the pores and 899 ms for the bulk sorbate. Unlike ^{13}C measurements, the T_1 relaxation times were determined by the 13-interval sequence.

Results and Discussion

Figure 2-2 presents ^{13}C and proton PFG NMR attenuation curves measured at 298 K for diffusion of methyl oleate in SBA-16-130. The measurements were performed for a range of diffusion times. Fig. 2-3 shows that the attenuation curves are not mono-exponential. This indicates that there is more than one ensemble of sorbate molecules characterized by the same diffusivity. It is also seen in the figure that the attenuation curves show some dependence on the effective diffusion time. Table 2-2 presents the result of fitting of the ^{13}C and ^{1}H PFG NMR attenuation curves using Equation 1.17 with n=2 or 3. ^{13}C PFG NMR attenuation curves can be fitted satisfactorily by assuming the presence of two ensembles of molecules, while 3 components are required to fit the proton PFG NMR attenuation curves. The absence of the third ensemble with the smallest diffusivity in the ^{13}C PFG NMR results is due to poor signal-to-noise ratios at high gradient amplitudes. Low signal-to-noise ratios are consequences of the low gyromagnetic ratio of ^{13}C nuclei and of the fact that the measurements were performed at natural abundance of ^{13}C nuclei. In addition to the ensemble diffusivities and their fractions Table 2-2 also presents the corresponding values of the square roots of the

mean square displacements (MSD). The MSD values were calculated using the Einstein relation (Equation 1.8).

The pattern of changing of the attenuation curves with increasing diffusion time is similar to that observed for the transition from the intra-crystalline diffusion (i.e. diffusion inside porous particles) to long-range diffusion (i.e. diffusion between many porous particles) in beds of zeolite crystals.[1,22]

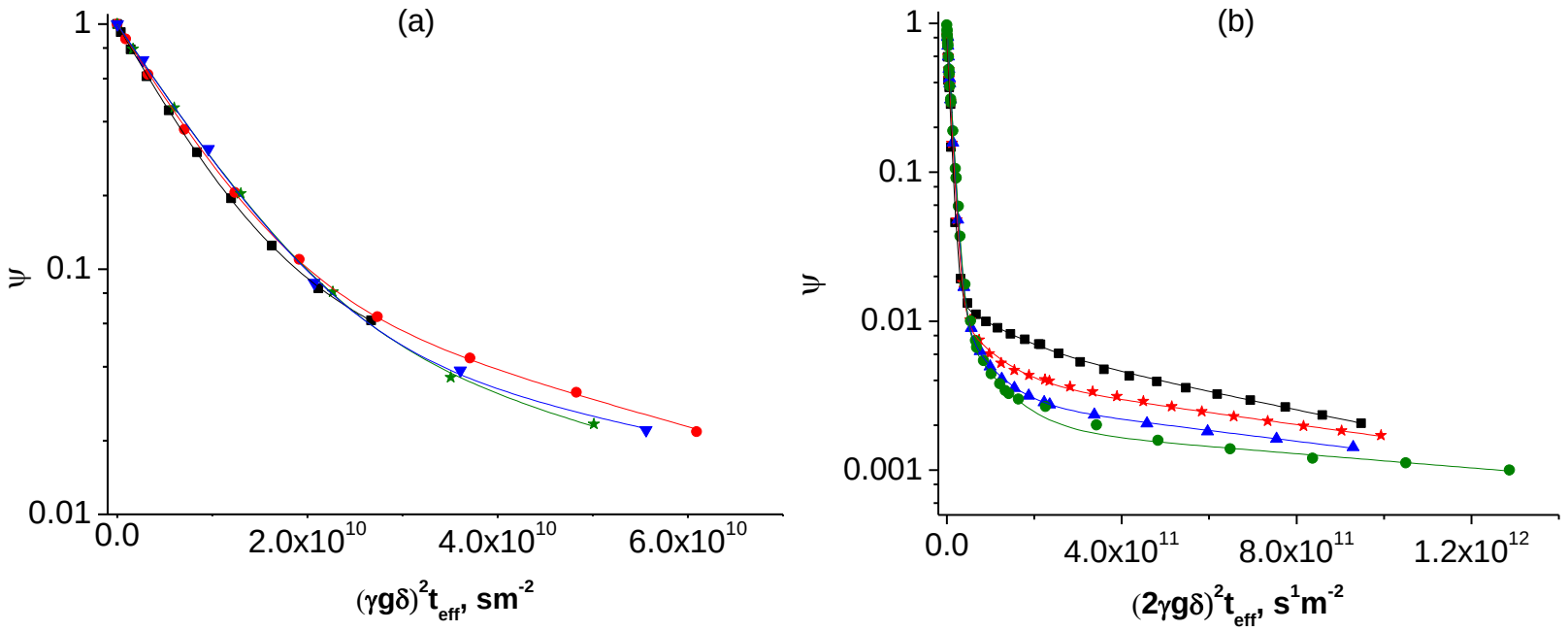

Figure 2-2. PFG NMR attenuation curves measured for diffusion of methyl oleate in the sample of SBA-16-130. The measurements were performed at T = 298 K. (a) ^{13}C PFG NMR attenuation curves for the following effective diffusion times: 3.8 ms (■), 8.7 ms (●), 18.7 ms (★), 38.7 ms (▼). Solid lines show the best fit curves obtained by using Equation 1.17 with n=2. (b) Proton PFG NMR attenuation curves for the following effective diffusion times: 7.5 ms (■), 31.5 ms (★), 63.5 ms (▲), 255.3 ms (●). Solid lines show the best fit curves obtained by using Equation 1.17 with n=3.

Table 2-2. Results of the fitting of ^{13}C and ^{1}H PFG NMR attenuation curves in Figure 2-2 by Equation 1.17 with n=2 or 3. The values of root MSD were obtained using Equation 1.8.

t_{eff} (ms)	D_1 (m^2/s)	p_1	$< r^2_1 >^{1/2}$ (μm)	D_2 (m^2/s)	p_2	$< r^2_2 >^{1/2}$ (μm)	D_3 (m^2/s)	p_3	$< r^2_3 >^{1/2}$ (μm)
				^{13}C PFG NMR Measurements					
3.8	$(1.7\pm0.2)\times10^{-10}$	0.89±0.04	2.0±0.1	$(2.8\pm1.2)\times10^{-11}$	0.11±0.04	0.8±0.1	N/A	N/A	N/A
8.7	$(1.6\pm0.2)\times10^{-10}$	0.90±0.05	2.9±0.2	$(2.5\pm1.2)\times10^{-11}$	0.10±0.03	1.1±0.1	N/A	N/A	N/A
18.7	$(1.4\pm0.1)\times10^{-10}$	0.93±0.06	4.0±0.2	$(2.3\pm1.0)\times10^{-11}$	0.07±0.02	1.7±0.1	N/A	N/A	N/A
38.7	$(1.4\pm0.1)\times10^{-10}$	0.94±0.06	5.7±0.3	$(1.8\pm1.0)\times10^{-11}$	0.06±0.02	2.1±0.1	N/A	N/A	N/A
				^{1}H PFG NMR Measurements					
7.5	$(1.6\pm0.2)\times10^{-10}$	0.98±0.05	2.7±0.2	$(7.3\pm4.0)\times10^{-12}$	0.010±0.001	0.6±0.1	$(1.3\pm0.1)\times10^{-12}$	0.010*	0.2±0.01
31.5	$(1.3\pm0.1)\times10^{-10}$	0.98±0.04	5.0±0.3	$(1.5\pm0.5)\times10^{-11}$	0.012±0.001	1.7±0.1	$(9.0\pm1.0)\times10^{-13}$	0.004*	0.4±0.02
63.5	$(1.2\pm0.1)\times10^{-10}$	0.98±0.04	6.8±0.3	$(1.8\pm0.5)\times10^{-11}$	0.014±0.001	2.6±0.2	$(8.3\pm0.8)\times10^{-13}$	0.003*	0.6±0.04
255.3	$(1.2\pm0.1)\times10^{-10}$	0.99±0.03	13.6±1.0	$(2.0\pm0.6)\times10^{-11}$	0.013±0.002	5.5±0.3	$(5.6\pm0.6)\times10^{-13}$	0.001*	0.9±0.06

*experimental uncertainty in the range of 10%

It is seen in Table 2-2 that the diffusivities of the ensembles 1 and 2 obtained by proton and ^{13}C PFG NMR are the same within the experimental uncertainty. This observed agreement allow us to rule out any types of artifacts, including disturbing influence of the magnetic susceptibility effects, in our diffusion data.

The first ensemble in Table 2-2 can be assigned to long-range diffusion based on the following consideration. It is seen that the fraction of this ensemble increases with increasing diffusion time and the root MSD values at higher diffusion times are much larger than the characteristic sizes of SBA-16-130. Also, the diffusivity of first ensemble is very close to the self- diffusivity of pure methyl oleate ($1.8 \times 10^{-10}\ m^2 s^{-1}$). This is true for both ^{13}C and ^{1}H PFG NMR measurements. From here on, focus will be on ^{1}H PFG NMR measurements as these measurements reports presence of all the ensembles. For the third ensemble, maximum value of the root MSD is 1 μm which is less than the characteristic size of SBA-16-130 and fraction of molecules decrease with the increasing effective diffusion time. Hence ensemble 2 corresponds to intraparticle diffusion. For the second ensemble, though the maximum root MSD value is larger than the characteristic size of the SBA-16-130, the diffusivity of this ensemble differs from the diffusivity of first ensemble by an order of magnitude. Hence, we can conclude that ensemble 2 represents diffusion of sorbate molecules that diffused part of the time inside the porous particles and part of the time in the liquid phase between the particles.

It is important to note that the observed dependencies of the PFG NMR attenuation curves on diffusion time can be affected by the longitudinal NMR relaxation process if the time constant of this process (T_1) for methyl oleate is smaller than or comparable with the diffusion time. For proton PFG NMR measurements, T_1 for fraction

of sorbate inside the pores is 49 ms which is comparable to the diffusion times used. Hence the fractions of the molecular ensembles diffusing inside the pores decrease with the increasing diffusion time due to longitudinal relaxation.

Based on the above discussion and results it can be concluded that intraparticle diffusivity of methyl oleate in SBA-16-130 is around $1.3x10^{-12}\ m^2s^{-1}$, i.e. the diffusivity of the ensemble 3 at the smallest diffusion time used.

Work in Progress

The presented study investigates transport in a single SBA-16 material. Work is currently in progress to study transport properties in different SBA-16 materials with different pore dimensions. Sorbates other than methyl oleate also need to be considered for transport studies to understand an effect of molecular size on transport properties.

CHAPTER 3
TRANSPORT IN CARBON MOLECULAR SIEVES

Carbon Molecular sieves (CMS) membranes are microporous amorphous structures formed by pyrolysis of a base polymer. The pores of CMS membranes consist of a distribution of selective ultra-micropores (< 6 Å) and slightly larger micropores (6 - 20 Å)[26,27]. Foley et al.[28] described the unique features and structural characteristics of carbon molecular sieves. Its structure is considered to be consisting of disordered graphitic platelets of carbon separated by interstitial spaces. The size of the gaps are determined by several factors, such as the presence of foreign atoms between the layers, hanging side groups, and cross-linking chains of carbon atoms. The presence of capping groups on the edges of the layers also influences the pore structure. CMS membranes are a promising class of materials for energy efficient separation of gas mixtures consisting of similarly sized molecules such as N_2/O_2 and CO_2/CH_4.[29,30]

Motivation

There has been a lot of research on transport in CMS membranes where the focus is on benchmarks relevant for applications, namely permeability and selectivity under specific conditions[26,27]. However, of interest is the ability to predict transport properties under all conditions and to understand how the complex pore structure of CMS membranes influences transport. This requires knowledge of self-diffusion in a broad range of length scales, including length scales as small 1 μm under well-defined conditions of loading, temperature, etc. Until now detailed microscopic studies of diffusion of light gases in a broad range of length scales inside CMS membranes are

not reported in the literature. This is the first study of self-diffusion in CMS membranes to our knowledge.

High field and high gradient PFG NMR was used to perform diffusion studies in CMS membranes. The PFG NMR measurements were carried out at different temperatures and for different diffusion times corresponding to different mean square displacements (MSDs) of sorbate molecules. The results reported below demonstrate that these measurements show high potential for uncovering the relationship between structural properties and transport in materials with a complex micropore structure.

Experimental Details

Materials and Sample Preparation

Three samples of carbon molecular sieves were supplied by the research group of Dr. William Koros from Georgia Institute of Technology. The three CMS samples investigated were- 6FDA/BPDA(1:1)-DAM CMS pyrolized in an inert gas (6FDA/BPDA), Matrimid® CMS pyrolized in an inert gas (Matrimid® Sample 1), and Matrimid® CMS pyrolized under vacuum (Matrimid® Sample 2). 6FDA/BPDA was synthesized as describe by Kiyono et al.[26] and Matrimid Sample 1 and Matrimid Sample 2 were obtained commercially.

PFG NMR samples were prepared in a 5 mm NMR tube. NMR tube with the sample inside was connected to the custom made vacuum system and samples were activated under high vacuum in the tube furnace at activation temperature of about 360 K for 24 hours. The sorbate used in this experiment was 99% isotopic purity ^{13}C methane purchase from Sigma-Aldrich. The samples were loaded with sorbate to an equilibrium pressure of 380 $\pm$ 5 torr and then sealed using a torch.

PFG NMR Measurements Details

Diffusion studies were performed by proton and ^{13}C PFG NMR using a wide-bore 17.6 T Bruker BioSpin spectrometer. Magnetic field gradients with the amplitude up to 30 T/m were generated using diff60 diffusion probe and Great60 gradient amplifier (Bruker BioSpin). Diffusion measurements were carried out using the 13-interval PFG NMR sequence with bipolar gradients[18-22] and the PFG NMR stimulated echo sequence with the longitudinal eddy current delay (PGSTE LED)[22,25]. The former sequence allows reducing or even completely eliminating the disturbing influence of magnetic susceptibility effects. Susceptibility effects are expected for heterogeneous porous materials such as stacks of membrane pieces studied in this work. The advantage of the latter sequence is related to the possibility of reducing influence of the transverse (T_2) NMR relaxation on the measured signal. For PGSTE LED sequence the absence of disturbing susceptibility effects and other measurement artifacts was confirmed by using the following two strategies: (1) it was verified that proton and ^{13}C PFG NMR diffusion data measured for the same diffusing species in the same samples and under the same conditions coincide within the experimental uncertainty, and (2) it was checked that an increase of the time interval between the first and second $\pi/2$ radiofrequency pulses of PGSTE LED sequence (while keeping the effective diffusion time constant) does not change the measured diffusivities. ^{13}C PFG NMR was employed in addition to the more traditional ^{1}H PFG NMR to take advantage of the longer ^{13}C T2 relaxation times that are typically observed for guest molecules confined in nanopores. The 13-interval and PGSTE LED sequences were used to measure PFG NMR attenuation curves, i.e. dependencies of the intensity of PFG NMR signal (A) on the amplitude of the magnetic

field gradient (g). The signal intensity was obtained by measuring amplitude of NMR lines of the sorbate molecules or area under these lines. The proton and ^{13}C NMR spectra of each type of sorbate consisted of a single line. It was verified that within the experimental uncertainty the line shape does not depend on the gradient amplitude. The PFG NMR attenuation curves provide direct information on effective diffusivities. Effective diffusivities D_i were obtained from monoexponential fit of the PFG NMR attenuation curves using Equation 1.17.

Results and Discussion

For all the measurements performed, it was observed that the PFG NMR attenuation curves show mono-exponential behavior in agreement with Equation1.17 where $n = 1$. This indicates that under any given measurement conditions used there is no significant distribution over methane self-diffusion coefficient inside membrane pieces of each studied membrane sample. It was also observed that the diffusion data for methane measured under the same conditions by ^{1}H and ^{13}C PFG NMR were identical within the experimental uncertainty. Figure 3-1 presents the proton and ^{13}C PFG NMR attenuation curves measured for diffusion of ^{13}C-labeled methane which coincide with each other. The agreement between the diffusivities measured at very different resonance frequencies of 750 and 188.6 MHz corresponding, respectively, to ^{1}H and ^{13}C nuclei provide strong evidence that the reported diffusion data are not distorted by the magnetic susceptibility effects or by any other disturbing effects.

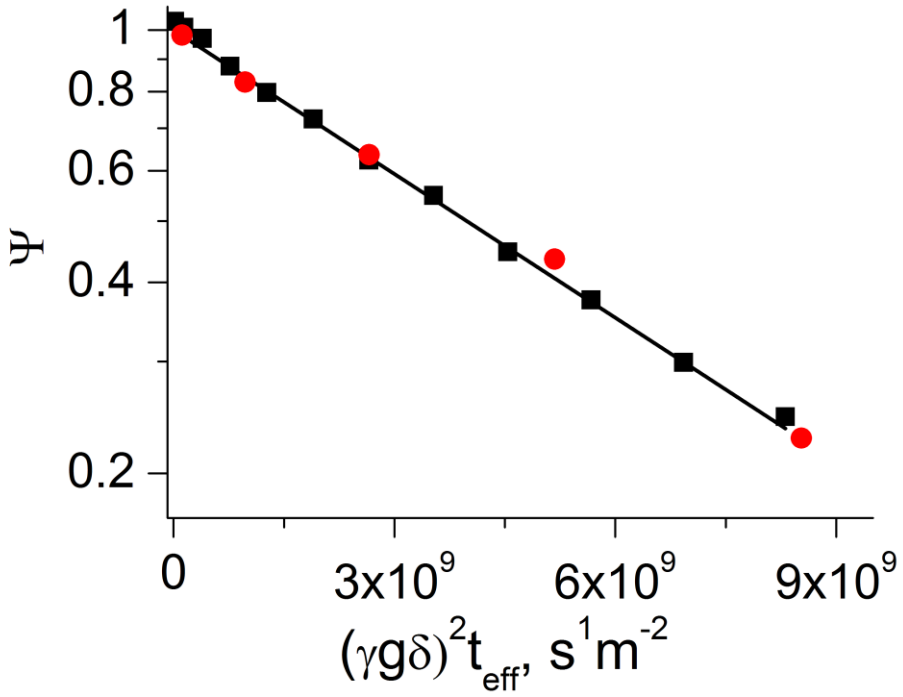

Figure 3-1. Examples of PFG NMR attenuation curves measured for methane diffusion in 6FDA/BPDA(1:1) -DAM CMS using proton (■) and ^{13}C (●) PFG NMR. The measurements were performed for the effective diffusion time of 9 ms at T = 321 K. The 13-interval and PGSTE LED PFG NMR pulse sequences were used for proton and ^{13}C measurements, respectively. The line shows the result of fitting both attenuation curves by Equation1.17 with $n = 1$.

Table 3-1 shows the methane diffusivities in CMS and the corresponding values of root MSD obtained by fitting the measured PFG NMR attenuation curves by Equation1.17 with $n = 1$ and Equation 1.8. The diffusion data are reported for the broad range of temperatures and effective diffusion times. In all cases the reported values of root MSD were much smaller than the smallest dimension (i.e. thickness $\approx$ 50μm) of the membrane pieces. It can be concluded that the measured diffusivities correspond to intra-membrane diffusion under conditions when the boundaries of the membrane pieces do not influence the diffusion behavior. Table 3-1 indicates that within the experimental uncertainty the intra-membrane diffusivities of methane do not change with increasing values of the root MSD. This is illustrated in Figure 3-2 which presents

examples of the measured dependencies of the methane diffusivities on the root MSD. These data demonstrate that the diffusion properties of the studied membranes remain homogeneous over a broad range of length scales starting with the length scales as small as 600 nm.

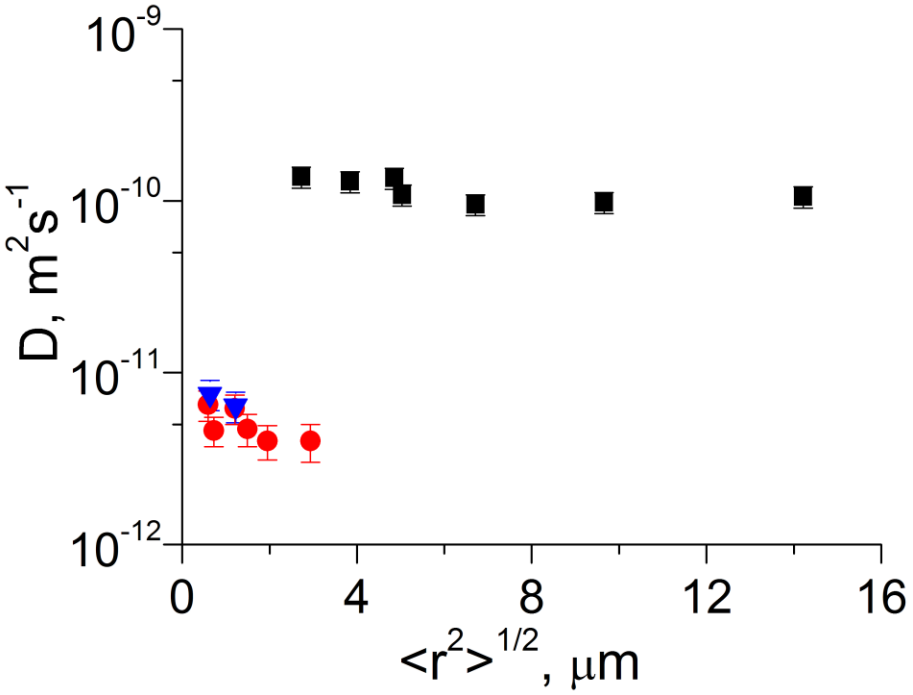

Figure 3-2. Dependences of the methane self-diffusion coefficient on the root MSD at T = 297 K for 6FDA/BPDA(1:1) -DAM CMS (■), Matrimid® CMS Sample 1 (●), and Matrimid® CMS Sample 2 (▼). The data was obtained using Equation 1.17 with $n = 1$ and Equation 1.8.

It is shown in Figure 3-3 that the temperature dependence of the methane self-diffusivity in the three membrane is in agreement with the Arrhenius law (Equation 3.1) which yields the estimated activation energies between 7-15 kJ/mol for the 6FDA/BPDA(1:1)–DAM CMS membrane sample and 3-14 kJ/mol for both Matrimid® CMS membrane samples.

$$D = A\, exp\left(-\frac{E_a}{RT}\right), \tag{3.1}$$

where A is the pre-exponential factor, E_a is the activation energy, T is the temperature and R is the gas constant. Within experimental uncertainty, the activation energies of all membranes are identical despite having different self-diffusivities. These results suggest that that the 6FDA/BPDA (1:1)–DAM CMS sample has a higher relative abundance of pores permeable to methane than both Matrimid® CMS samples.

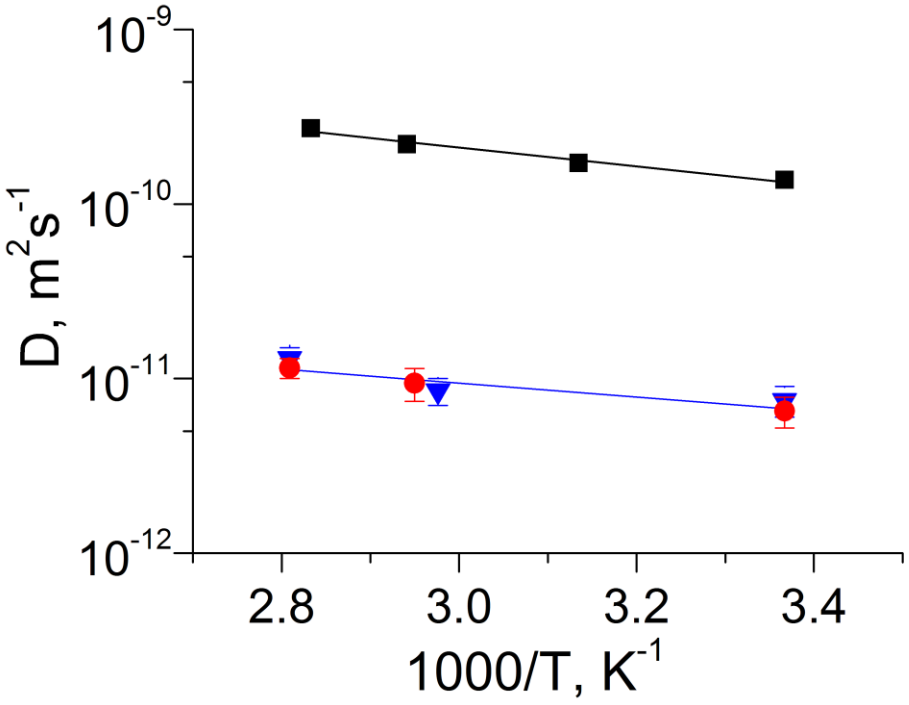

Figure 3-3. Temperature dependences of the methane self-diffusion coefficient measured by PFG NMR for the effective diffusion time 9 ms in 6FDA/BPDA(1:1) -DAM CMS (■), Matrimid® CMS Sample 1 (●), and Matrimid® CMS Sample 2 (▼).

Table 3-1. Results of the fitting of ^{13}C and ^{1}H PFG NMR attenuation curves for methane diffusion in: 6FDA/BPDA-DAM(1:1), Matrimid® Sample 1 and Sample 2.

Sample	***T*(K)**	t_{eff} **(ms)**	***D*** **(m^2s^{-1})**	**Root MSD (μm)**
6FDA/BPDA-DAM carbon molecular sieve loaded with methane	297	9	$(1.4 \pm 0.2) \times 10^{-10}$	2.7 ± 0.2
		19	$(1.3 \pm 0.2) \times 10^{-10}$	3.8 ± 0.3
		29	$(1.4 \pm 0.2) \times 10^{-10}$*	4.9 ± 0.3
		39	$(1.1 \pm 0.2) \times 10^{-10}$	5.0 ± 0.3
		79	$(9.5 \pm 1.3) \times 10^{-11}$	6.7 ± 0.5
		159	$(9.8 \pm 1.4) \times 10^{-11}$*	9.7 ± 0.7
		319	$(1.1 \pm 0.1) \times 10^{-10}$*	14 ± 1
	319	9	$(1.7 \pm 0.2) \times 10^{-10}$	3.0 ± 0.2
		19	$(1.5 \pm 0.2) \times 10^{-10}$	4.1 ± 0.3
		39	$(1.5 \pm 0.2) \times 10^{-10}$	5.9 ± 0.4
	340	9	$(2.2 \pm 0.3) \times 10^{-10}$	3.4 ± 0.2
		19	$(2.2 \pm 0.3) \times 10^{-10}$	5.0 ± 0.3
		39	$(2.0 \pm 0.3) \times 10^{-10}$	6.8 ± 0.5
	353	9	$(2.7 \pm 0.4) \times 10^{-10}$	3.8 ± 0.3
		19	$(2.6 \pm 0.4) \times 10^{-10}$	5.4 ± 0.4
		39	$(2.4 \pm 0.3) \times 10^{-10}$	7.5 ± 0.5
Matrimid® carbon molecular sieve loaded with methane (1)	297	9	$(6.5 \pm 1.3) \times 10^{-12}$	0.6 ± 0.06
		19	$(4.6 \pm 0.9) \times 10^{-12}$	0.7 ± 0.1
		39	$(6.2 \pm 1.2) \times 10^{-12}$	1.2 ± 0.1
		79	$(4.7 \pm 1.0) \times 10^{-12}$	1.5 ± 0.2
		159	$(4.0 \pm 0.9) \times 10^{-12}$	2.0 ± 0.2
		359	$(4.0 \pm 1.0) \times 10^{-12}$	2.9 ± 0.4
	339	9	$(9.4 \pm 2.0) \times 10^{-12}$	0.7 ± 0.07
	356	9	$(1.2 \pm 0.2) \times 10^{-11}$	0.8 ± 0.05
Matrimid® carbon molecular sieve loaded with methane (2)	297	9	$(7.5 \pm 1.5) \times 10^{-12}$	0.6 ± 0.1
		39	$(6.4 \pm 1.3) \times 10^{-12}$	1.2 ± 0.1
	336	9	$(8.5 \pm 1.5) \times 10^{-12}$	0.7 ± 0.1
	356	9	$(1.3 \pm 0.2) \times 10^{-11}$	0.8 ± 0.1

Diffusivity values were obtained using Equation 1.17 with $n = 1$. The values of root MSD were obtained using Equation 1.8. Results correspond to diffusion measurements at different temperatures (*T*) and effective diffusion times (t_{eff}). The data obtained by ^{13}C PFG NMR are labeled by (*). Rest of the data was obtained by ^{1}H PFG NMR

It is seen in Figure 3-3 that for any temperature used the methane self-diffusivity in 6FDA/BPDA is about an order of magnitude higher than in that in Matrimid Sample 1 and Matrimid Sample 2. At the same time, the corresponding methane diffusivities in the latter two samples were found to be the same within the experimental uncertainty. This observation is consistent with the expectation of a smaller average pore size and narrower distribution over pore sizes in Matrimid Sample 1 and Matrimid Sample 2 in comparison with those in 6FDA/BPDA[26].

Work in Progress

Diffusion studies with CO_2 as sorbate molecule in the 6FDA/BPDA and Matrimid® CMS samples are in progress. Further, investigation of transport properties for a mixture of CH_4/CO_2 is necessary to obtain selectivity information. Also, effect of different loadings on transport properties needs to be investigated.

LIST OF REFERENCES

(1) Kärger, J.; Ruthven, D. M. Diffusion in zeolites and other microporous solids; Wiley New York, 1992.

(2) Fick, A. E. Ann. Phys. 1855, 94, 59.

(3) Fick, A. E. Phil. Mag. 1855, 10, 30.

(4) Crank, J. The Mathematics of Diffusion; Oxford University Press: New York, 2004.

(5) Kärger, J.; Vasenkov, S.; Auerbach, S. M. Diffusion in Zeolites. In Handbook of Zeolite Science and Technology; Auerbach, S. M., Carrado, K. A., Dutta, P. K., Eds.; Marcel Dekker, Inc.: New York, Basel, 2003; pp 341.

(6) Levitt, M. H. Spin dynamics : basics of nuclear magnetic resonance; John Wiley & Sons: Chichester ; New York, 2001.

(7) Keeler, J. Understanding NMR spectroscopy, 2nd ed.; John Wiley and Sons: Chichester, 2010.

(8) Levitt, M. H. Spin dynamics : basics of nuclear magnetic resonance, 2nd ed.; John Wiley & Sons: Chichester, England ; Hoboken, NJ, 2008.

(9) Callaghan, P. T. Principles of nuclear magnetic resonance microscopy; Clarendon Press: New York, 1991.

(10) Gibbs, S. J.; Johnson, C. S. Journal of Magnetic Resonance (1969) 1991, 93, 395.

(11) Cho, E. B.; Kim, D.; Górka, J.; Jaroniec, M. J. Mater. Chem. 2009, 19, 2076.

(12) Tanner, J. E. Journal of Chemical Physics 1970, 52, 2523.

(13) Stallmach, F.; Galvosas, P. Spin Echo NMR Diffusion Studies. In Annual Reports on NMR Spectroscopy; Webb, G. A., Ed.; Academic Press, 2007; Vol. Volume 61; pp 51.

(14) Hahn, E. L. Physical Review 1950, 80, 580.

(15) Carr, H. Y.; Purcell, E. M. Physical Review 1954, 94, 630.

(16) Stejskal, E. O.; Tanner, J. E. Journal of Chemical Physics 1965, 42, 288.

(17) Tanner, J. E. Review of Scientific Instruments 1965, 36, 1086.

(18) Cotts, R. M.; Hoch, M. J. R.; Sun, T.; Markert, J. T. J. Magn. Reson. 1989, 83, 252.

(19) Galvosas, P.; Stallmach, F.; Seiffert, G.; Kärger, J.; Kaess, U.; Majer, G. J. Magn. Reson. 2001, 151, 260.

(20) Wu, D. H.; Chen, A. D.; Johnson, C. S. Journal of Magnetic Resonance, Series A 1995, 115, 260.

(21) Wider, G.; Dotsch, V.; Wuthrich, K. Journal of Magnetic Resonance, Series A 1994, 108, 255.

(22) Zhao, D. Y.; Feng, J. L.; Huo, Q. S.; Melosh, N.; Fredrickson, G. H.; Chmelka, B. F.; Stucky, G. D. SCIENCE 1998, 279, 548.

(23) Sakamoto, Y.; Kaneda, M.; Terasaki, O.; Zhao, D. Y.; Kim, J. M.; Stucky, G.; Shin, H. J.; Ryoo, R. Nature 2000, 408, 449.

(24) Serra, E.; Mayoral, Á.; Sakamoto, Y.; Blanco, R. M.; Díaz, I. Microporous and mesoporous materials 2008, 114, 201.

(25) Gibbs, S. J.; Johnson Jr., C. S. J. Magn. Reson. 1991, 93, 395.

(26) Kiyono, M.; Williams, P. J.; Koros, W. J. Carbon 2010.

(27) Suda, H.; Haraya, K. Chem. Commun. 1997, 93.

(28) Foley, H. C. Microporous Materials 1995, 4, 407.

(29) Ismail, A. F.; David, L. Journal of membrane science 2001, 193, 1.

(30) Bernardo, P.; Drioli, E.; Golemme, G. Industrial & Engineering Chemistry Research 2009, 48, 4638.

BIOGRAPHICAL SKETCH

Rohit Kanungo was born in 1986 at Jaipur, India to Prem Prakash and Beena Kanungo. He grew up there with his parents and younger brother Parth Kanungo and all his early schooling was done in Jaipur. He attended the University Institute of Chemical Engineering and Technology (formerly DCET), Panjab University, Chandigarh, India and earned a Bachelor of Chemical Engineering in 2008. Then, he worked as a Process Engineer at Samsung Engineering India Pvt. Ltd. Noida, India for 18 months. In January 2010 he enrolled at University of Florida (UF), Gainesville and earned a Master of Science in chemical engineering in 2011.